Sensing abilities of embedded vertically aligned carbon nanotube forests in structural composites: From nanoscale properties to mesoscale

Composites Part B 255 (2023) 110587

Contents lists available at ScienceDirect

Composites Part B

journal homepage: www.elsevier.com/locate/compositesb

Sensing abilities of embedded vertically aligned carbon nanotube forests in structural composites: From nanoscale properties to mesoscale functionalities

Tobias Karlsson [a,*], Per Hallander [a,b], Fang Liu [c], Thirza Poot [d], Malin Åkermo [a]

[a] Department of Engineering Mechanics, KTH Royal Institute of Technology, Stockholm, Sweden
[b] SAAB AB, Linköping, Sweden
[c] Department of Industrial and Materials Science, Chalmers University of Technology, Gothenburg, Sweden
[d] Department of Physics, Chemistry and Biology, Linköping University, Linköping, Sweden

ARTICLE INFO

Handling Editor: Prof. Ole Thomsen

Keywords:
Multifunctionality
A. Polymer-matrix composites (PMCs)
A. Nano-structures
B. Electrical properties

ABSTRACT

In this paper, Vertically Aligned Carbon Nanotube (VACNT) forests are embedded into two different glass fibre/epoxy composite systems to study their sensing abilities to strain and temperature. Through a bottom-up approach, performing studies of the VACNT forest and its individual carbon nanotubes on the nano-, micro-, and mesoscale, the observed thermoresistive effect is determined to be due to fluctuation-assisted tunnelling, and the linear piezoresistive effect due to the intrinsic piezoresistivity of individual carbon nanotubes. The VACNT forests offer great freedom of placement into the structure and reproducibility of sensing sensitivity in both composite systems, independent of conductivity and volume fraction, producing a robust sensor to strain and temperature.

1. Introduction

Since their discovery, carbon nanotubes (CNTs) have been widely studied [1]. Their electrical properties have in particular proved to be complex. The chirality of single-walled CNTs (SWCNT) has been seen to determine whether the electronic structure is semiconducting, metallic, or quasi-metallic. In addition to this, the band gap of each semiconducting SWCNT depends on the tube diameter, decreasing as the diameter increases [2,3]. In individual CNTs, excellent current capacity has been observed, surpassing the most conductive metals, making CNTs interesting for power circuits. This impressive current capacity of individual CNTs has been determined to be due to ballistic conduction [4]. Ballistic conduction has been reported in both metallic [5–7] and semiconducting [8,9] SWCNTs as well as in multi-walled CNTs (MWCNT) [10–13]. However, diffusive conduction has also been observed in experiments with MWCNTs [5,14]. By definition, the electron mean free path must be longer than the conduction channel, i.e. the CNT, to have ballistic conduction in the CNT. The electron mean free path in a CNT depends on its structure, increasing with an increase in diameter [7], and decreasing with the number of dislocations and impurities, acting as scattering sites [15]. MWCNTs, which could be seen as containing several concentric SWCNTs, have an electronic behaviour depending on their constituent tubes. In addition, internal resistance between each tube [16] is present in MWCNTs. However, it has been seen that most individual MWCNTs exhibit metallic properties [17,18]. More concisely, individual CNTs may be widely different from each other and are currently difficult to clearly define in production processes.

The electrical properties of larger architectures of CNTs have more predictive behaviour, their properties being more dependent on the concentration and aspect ratio of CNTs, relating to percolation theory and associated tunnelling conditions. The issues previously described related to the use of individual CNTs may thus be mitigated. These architectures of CNTs may be in the form of threads and yarns [19], buckypapers [20,21], nanocomposites [22–26], forests [27–29] or coatings [30–32], which can be used for sensing.

* Corresponding author.
E-mail address: Tobiask2@kth.se (T. Karlsson).

https://doi.org/10.1016/j.compositesb.2023.110587
Received 26 September 2022; Received in revised form 23 January 2023; Accepted 2 February 2023
Available online 9 February 2023

Different CNT architectures have been evaluated as sensing elements for strain [23–26,31], temperature [20,22,28,29,33], pressure [19,27,30], humidity [34], and cure monitoring of thermoset polymers [21,31,32], studying their electroresistive behaviour in response to the mentioned stimuli. Aspect ratio of individual CNTs, and the morphology and concentration of CNTs in these CNT architectures collectively affect their resistive response to stimuli. Work remains to map out how the different CNT architectures function as sensors to different stimuli. Consequently, more architectures of CNTs and their sensing abilities must be studied.

Due to their high specific modulus, strength, and corrosive properties, fibre-reinforced polymer composites (FRPCs) have found increased use in the aerospace, automotive, civil, and marine sectors. In addition, unlike previous metallic components, the use of FRPCs enables the embedment of sensors into the structure due to their manufacturing methods. However, when designing a sensor for embedment into the composite structure, the sensor's size is critical to not interfere with, or deteriorate, the mechanical structure. Ideally, a non-intrusive multi-purpose sensor embedded into the composite structure is desired, which may first be used for *in-situ* online cure monitoring during production, and later in the cured state used for structural health monitoring (SHM). Cases of CNT architectures embedded in FRPCs have been reported, monitoring strain for SHM:

Boztepe et al. [35] embedded buckypaper into a carbon fibre/epoxy composite, insulating the buckypaper electrically from the conductive carbon fibre layers with an epoxy adhesive film, ensuring conduction through the buckypaper. The buckypaper performed sensing during fatigue testing up to 10.000 cycles, the piezoresistive response drifting throughout the test. However, the form of the response signal remained the same, exhibiting an initial negative parabolic piezoresistive response, until 0.4% strain. This was caused by the Poisson effect compressing the buckypaper. Thereafter, a positive and linear piezoresistive behaviour sets in. Similarly, Aly et al. [36] studied embedded aligned buckypapers in glass fibre/epoxy composite to perform damage detection and strain monitoring. They studied the influence of plasma treatment, pre-straining, and stacking of several buckypapers, prior to embedment, on the piezoresistive response. A negative linear piezoresistive response until 0.6% strain was measured, again due to the Poisson effect, before transitioning into a positive linear piezoresistivity until failure. The shift of the piezoresistive behaviour was argued to be due to the piezoresistivity of individual CNTs, damage accumulation in the sample and a decrease in contact points between the stacked buckypapers. Luo et al. [31] studied SWCNT-coated fibres for lifelong sensing in FRPCs. Through a spray coating method, SWCNTs were coated on the surface of glass, polyaramid and nylon fibres. All fibres were embedded into an interlaminar region of glass fibre/epoxy prepreg laminates and were able to monitor the curing of the lamina. Interestingly, the sensor showed different piezoresistive behaviour depending on its placement in relation to the applied load. In alignment with the load, the transverse compressive load due to the Poisson effect caused a negative piezoresistivity due to the decrease of inter-tube distance between CNTs in the resin-infiltrated CNT coating. Similarly, when placed perpendicular to the applied load, the resulting tensile strain in the fibre's transverse direction causes an increase of the inter-tube distance, causing a positive piezoresistivity. From these studies, it is clear that the architecture of the CNT network is of paramount importance to its piezoresistive response. Therefore, the sensing abilities of more CNT architectures need to be studied. One such architecture is vertically aligned CNT (VACNT) forests. The effects on the mechanical properties when embedding VACNT forests to structural composites has been studied, causing no deterioration to its mechanical properties [37,38]. Therefore, VACNT forests are a suitable CNT architecture for embedment into structural composites and their sensing abilities should be studied.

This paper evaluates the sensing abilities for temperature and strain of VACNT forests embedded into glass fibre/epoxy composite. The studied VACNT forest is relatively simple to manufacture and straightforward to distribute into the resin, offering great freedom of placement in the composite structure to provide localized sensing possibilities. Consequently, the distribution of the VACNT forest into the resin causes its sensing abilities to depend on the matrix once cured. A bottom-up approach has been adopted in this paper to explain the sensing abilities of the manufactured coupons on the mesoscale. Initiating on the nanoscale, individual CNTs from the VACNT forest are studied through transmission electron microscopy (TEM), and the nano-morphology of the VACNT forest is studied through scanning electron microscopy (SEM). The microscale studies include the use of optical microscopy, quantifying deposition coverage of the VACNT forest to the prepreg surface, and the micro-morphology of the CNT-rich region after curing. Finally, the mesoscale trials consist of all experiments performed on the manufactured coupons, including electrical characterization, temperature measurements and strain measurements, revealing good sensing abilities. This bottom-up approach makes it possible to explain the origins of the observed conduction mechanism, thermoresistive and piezoresistive behaviour on the mesoscale down to the micro- and nanoscale.

2. Experimental

The experimental work is divided into the sample manufacturing and characterization. The sample manufacturing presents the VACNT forest deposition onto prepreg surfaces and the subsequent curing of samples. In the characterization, a bottom-up approach has been adopted.

2.1. Material

The studied nanomaterial, 20 μm high VACNT forests was manufactured by N12 Technologies. Grown on stainless steel substrates, the VACNT forests were delivered still attached to the substrate and were used without further modification. Two glass fibre/epoxy prepregs were used in this study. The first, HexPly 6376-G-120 glass fibre prepreg from Hexcel, which is from now on related to as 6376-prepreg. The 6376-prepreg has a glass fibre volume of 42%, woven in a 4-harness satin weave, HexForce 120. The second, DeltaPreg W105P/DT806W glass fibre prepreg from DeltaTech, which is from now on related to as DeltaTech-prepreg. This prepreg uses a W105P plain weave and has a glass fibre volume fraction of 48%. To establish electrical contact with the embedded VACNT forest, a non-woven carbon fibre veil (Carbon 20301A, 34 g/m^2, Technical Fibre Products Ltd) was chosen as contacting material.

2.2. Sample manufacturing

2.2.1. Deposition of VACNT forest

To successfully embed the VACNT forests into the composite structure, the VACNT forest was first deposited on the surface of a prepreg. The deposition makes use of capillary forces to infiltrate the inter-tube space between the CNTs with epoxy, requiring both increased temperatures and pressure. The deposition was performed in a set-up consisting of a heating plate, encapsulated by a vacuum bag connected to a vacuum pump. Using this set-up, both temperature and vacuum can be controlled. To deposit the VACNT forest, the prepreg was placed on top of the heating plate followed by the stainless-steel substrate on top of the prepreg, with the VACNT forest facing the prepreg surface. Thereafter the vacuum bag was sealed. The deposition procedure of the VACNT forest to the surface of the 6376-prepreg was initiated by increasing its temperature to 55 °C, using the heating plate. Upon reaching temperature, 890 mbar vacuum was applied and held for 2 min, pressing the VACNT forest and substrate down to the surface of the prepreg. After this, the vacuum bag was opened and the stainless-steel substrates were removed, leaving the VACNT forest deposited on the prepreg surface (Fig. 1), infiltrated by epoxy. During the deposition of the VACNT forests

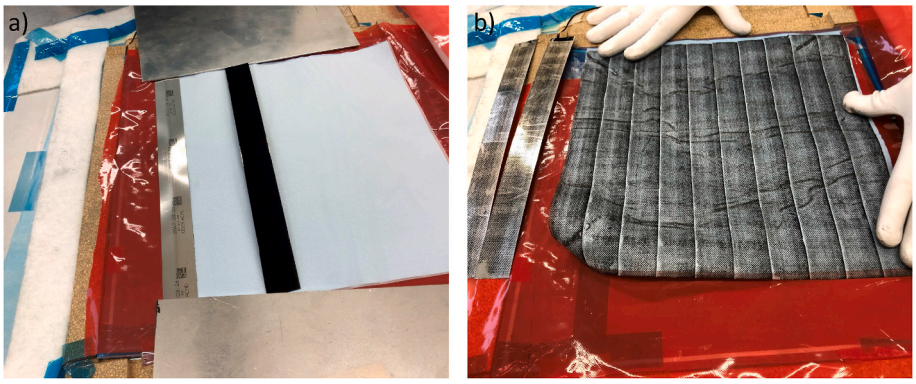

Fig. 1. a) The as-grown VACNT-forest attached on the stainless-steel substrate, on top of a 6376-prepreg. b) The 6376-prepreg after deposition of VACNT forest to the surface.

to the DeltaTech-prepreg, the temperature was elevated to 35 °C, after which a vacuum of 300 mbar was applied for a few seconds.

2.2.2. Curing of samples

The prepared samples consisted of 20 layers of prepreg material, with the in-plane dimensions being 250 × 30 mm. Prepregs with VACNT forests deposited on the surface were placed during the lay-up of the lamina to be positioned towards the midplane of the lamina. Two sample designs were used in this work, each design manufactured using two prepreg systems, resulting in four sample types. One sample design used one prepreg with deposited VACNT forests on the surface to face the midplane. The second sample design used two prepregs with VACNT forest deposited to the surface, their surfaces meeting each other in the midplane of the lamina, see Fig. 2. To contact the VACNTs in the midplane, carbon fibre veil contacts were inserted 30 mm into the midplane of the lamina from each side during the lay-up. Consequently, the potential is applied across the VACNT forest, perpendicular to the forest alignment. The curing of the sample was performed out-of-autoclave, inside a vacuum bag (600 mbar), placed inside an ACS FM340C climate chamber. The climate chamber was used to control the ramping of temperature. The cure cycle of the 6376-prepreg consisted of an initial temperature ramp of 2 °C/min up to 180 °C, followed by a 2 h dwell at 180 °C before cooling down to room temperature slowly. The cure cycle of the DeltaTech-prepreg consisted of an initial temperature ramp of 2 °C/min up to 65 °C, where it was kept for 16 h. Thereafter, a post-cure at 120 °C, for 1 h followed before cooling down. Four sample types were manufactured and named: 6376-1 CNT and DeltaTech-1 CNT, containing one VACNT forest in the midplane; and 6376-2 CNT and DeltaTech-2 CNT, containing two VACNT forests in the midplane.

2.3. Characterization

Starting on the nanoscale, individual CNTs are investigated with TEM in a statistical study, determining the number of walls and their thickness. The VACNT forest is later studied with SEM, determining the height of the forest. Later, the areal weight of the VACNT forest is determined through TGA. Combining the results from TEM, SEM and TGA, the volume fraction of CNTs in the forest is calculated, assuming the CNTs as solid cylinders and using the density of graphite. This approach has previously been used by Hart et al. [39]. The characterization transitions hereafter to the microscale, evaluating and quantifying the deposition of the VACNT forest on prepreg surfaces and studying the morphology of the VACNT forest in the cured lamina using optical microscopy and image analysis. Finally, measurements on the mesoscale were performed. Current-voltage sweeps, stability of resistance, temperature and strain sensing measurements are presented for each sample type.

2.3.1. Scanning electron microscopy (SEM)

The as-produced VACNT forests were studied using a Zeiss LEO 1550 SEM instrument with a Schottky field emission gun in a GEMINI column. The VACNT forest samples were mounted on pin mount specimen holders using conductive copper SEM tape. Micrographs were acquired using an in-lens secondary electron detector with an accelerating voltage of 3 kV. The morphology of the infused VACNT forest on the glass fibre prepreg was analyzed with a Zeiss LEO Ultra 55 SEM. The

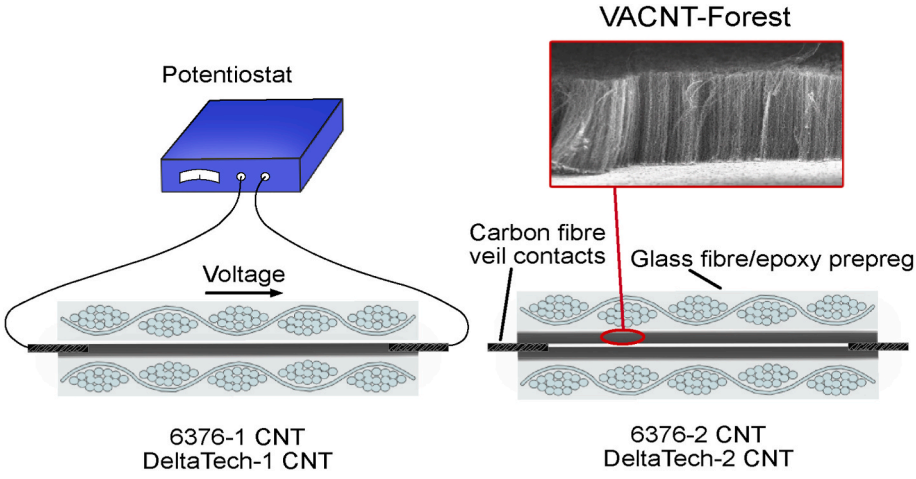

Fig. 2. The four sample types studied in this work, using one or two VACNT forest deposited prepreg surfaces in the midplane.

accelerating voltage was 5 kV. Secondary electron micrographs were acquired using the Everhart-Thomley (low magnification) or in-lens (high magnification) secondary electron detector.

2.3.2. Transmission electron microscopy (TEM)

Carbon nanotubes were first carefully removed from the steel substrate with a clean plastic spoon. They were then transferred to a 20 ml glass bottle, which was filled with 10 ml 2-propanol. The glass bottle was then ultrasonic agitated for 30 min, and a well-suspended uniform suspension was obtained. Then a drop of suspension was transferred onto a 3 mm TEM specimen grid with a thin coated carbon film (holey carbon grid) using a pipette; a filter paper was used to remove the extra liquid. Finally, after drying in air, a TEM specimen was ready. A FEI Titan 80–300 transmission electron microscope equipped with a field emission gun was used for imaging the carbon nanotubes. In order to mitigate electron radiation damage on the carbon nanotubes, an accelerating voltage of 80 kV was used [40].

2.3.3. Thermal gravimetric analysis (TGA)

The areal weight of the VACNT forests was determined using a TGA, Mettler Toledo TGA/DSC 3+. The VACNT forest sample was studied up to 800 °C, increasing the temperature 10 °C/min, with a flow of 20 ml/min of oxygen gas.

2.3.4. Optical microscopy

Optical Microscopy, using an OLYMPUS BX53 M microscope with an OLYMPUS UC90 colour camera, was used to: a) quantify the deposition of the VACNT forest to the prepreg surface, and b) study the morphology of the VACNT forests after curing of samples. To quantify the VACNT forest deposition, micrographs of prepreg surfaces were acquired, and subsequently image processed and analyzed in MATLAB. In MATLAB, the RBG images were converted to grayscale and later applied a threshold to divide the pixels into black (VACNT forest deposition on prepreg surface) and white (non-deposited prepreg surface) pixels, quantifying the areal coverage of deposited VACNT forests. To study the VACNT forest after curing, samples were cut and polished to study the cross-section of the laminas.

2.3.5. Electrical characterization

Electrical measurements, using a potentiostat (SP-50, BioLogic), were performed on the manufactured samples in the cured state. First, current-voltage measurements were performed by a voltage sweep between −10 and 10 V. Secondly, stability measurements under constant voltage, 10 V, were performed for 100 h.

2.3.6. Temperature sensing

Thermoresistive measurements were carried out on each sample type. The tests were performed inside an ACS FM340C climate chamber, studying the temperature from −70 °C to 180 °C. Using the SP-50 potentiostat to apply a constant voltage, the change in resistance was calculated.

2.3.7. Strain sensing

All four sample types were equally tested, studying their piezoresistive response to strain. An electromechanical tensile machine, Instron 4505, was used during the study. Applying a constant voltage to the samples using the SP-50 potentiostat, their resistive response to strain was calculated. A digital image correlation (DIC) method was used to measure strains during testing, using a GOM camera system and Aramis software package. Painting a speckle pattern on the surface of the specimen, this accurate 2D image analysis technique can record the displacement in both x- and y-axis of the sample by tracking the speckle pattern. Two trials of mechanical testing were performed: a) Two load cycles 0–10 kN, 50 N/s with 30 s hold between load and offload and vice versa, b) Progressive load increase 0–1 kN in steps of 100 N. These two ranges were selected in order to i) study the strain sensing behaviour and sensitivity in the linear-elastic region of the material, ii) determine a lower boundary of possible sensing.

3. Results

This section presents the results obtained by the previously described methodology. Initiating on the nanoscale, the VACNT forest and its constituent tubes prior to embedment are characterized. Later, on the microscale, the VACNT forest's deposition onto prepregs and micromorphology in the cured lamina is studied. Combining the nano- and microscale results, the volume fraction in the CNT-containing region is determined. Finally, current-voltage, temperature, and strain sensing measurements on the manufactured samples were performed, characterizing the sensing abilities on the mesoscale.

3.1. Volume fraction determination of VACNT forest

The VACNT forest height was determined to be 20 μm through SEM, see Fig. 3a, studying the forest whilst still attached to the substrate. The alignment of the CNTs is seen in the figure, verifying the forest to have a good vertical alignment. In Fig. 3b, a TEM picture of an individual CNT from the VACNT forest is seen. Using TEM, 150 individual CNTs were studied, measuring their inner and outer diameters, and determining their number of walls. The CNTs in the VACNT forest are determined to have 7 ± 2 walls, with an inner diameter of 5.5 ± 2 nm and an outer diameter of 8 ± 2 nm.

Performing TGA, see figure S1 in Supportive Information, it is observed that 12.5 wt% of the VACNT forest is lost before reaching 400 °C. This loss of mass is due to amorphous carbon in the VACNT forest oxidizing [41]. CNT oxidization initiates at 450 °C and continues rapidly until 620 °C [41–44]. The mass loss observed between 450 and 620 °C is used in the subsequent calculations. Using 8 nm as the outer diameter and approximating the CNTs as solid cylinders, the volume fraction of CNTs in the VACNT forest is calculated to be 0.4% on the substrate, equalling an areal density of $6.8*10^9$ CNTs/cm^2.

Through optical microscopy and subsequent image analysis, the area of the prepreg surface covered by the deposited VACNT forest is determined. The amount of CNTs in each sample is therefore possible to calculate, by combining the determined area and the volume fraction of the CNTs in the VACNT forest. The surfaces of 6376-prepreg and DeltaTech-prepreg with deposited VACNT forest are seen in Fig. 4a and c, together with performed image treatment to separate deposited and non-deposited area. The deposition parameters for each prepreg have been optimized for maximal VACNT forest deposition. The VACNT forest is determined to cover 65.95% (std 2.20) and 94.39% (std 1.52) of the areas of the 6376- and DeltaTech-prepregs, respectively. The difference in deposited area of VACNT forest is due to the difference in topology of the two prepreg surfaces, caused by the weaving patterns; 4-harness satin weave of the 6376-prepreg and plain weave of the DeltaTech-prepreg. As the VACNT forest is deposited by infiltration of epoxy through capillary forces, physical contact between prepreg and VACNT forest is required. In Fig. 4a, it is seen that the deposited area is mainly on the warp of the weave as physical contact has only been achieved here during the deposition process. The plain weave of the DeltaTech-prepreg, Fig. 4c, provides a smoother surface, therefore achieving more contact between the VACNT forest and prepreg epoxy during the deposition. The observed rhombic pattern of the non-deposited area is caused by the prepreg's protective film having this pattern, creating an indentation on the surface.

Micrographs are presented in Fig. 5 of cross-sections from a) 6376-1 CNT and b) 6376-2 CNT. The CNT-rich region is observed to be non-continuous, being interrupted by glass fibres and having an average thickness of 47.13 μm (21.89 std) and 44.38 μm (19.49 std) in the 6376-1 CNT and 6376-2 CNT samples, respectively. Further, the CNT-rich region in Fig. 5a and b is seen to be non-uniform, having varying thickness and waviness. This implies changes to the original vertical

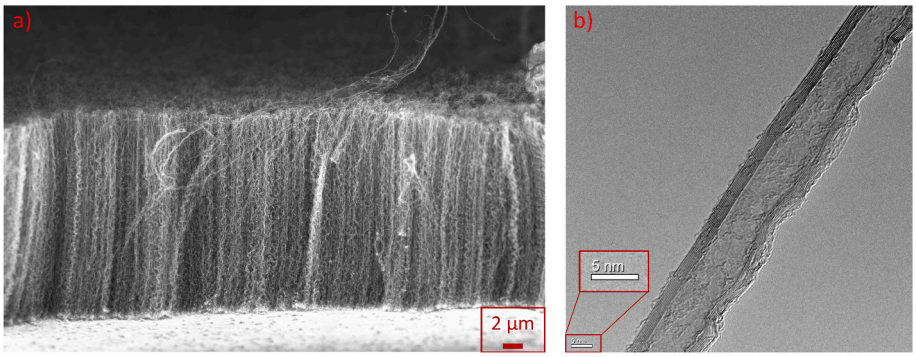

Fig. 3. a) SEM of the VACNT forest still attached to the stainless-steel substrate. Credit to Thirza Poot at Linköping University. b) TEM picture of individual CNT from the VACNT forest. Credit to Fang Liu at Chalmers University of Technology.

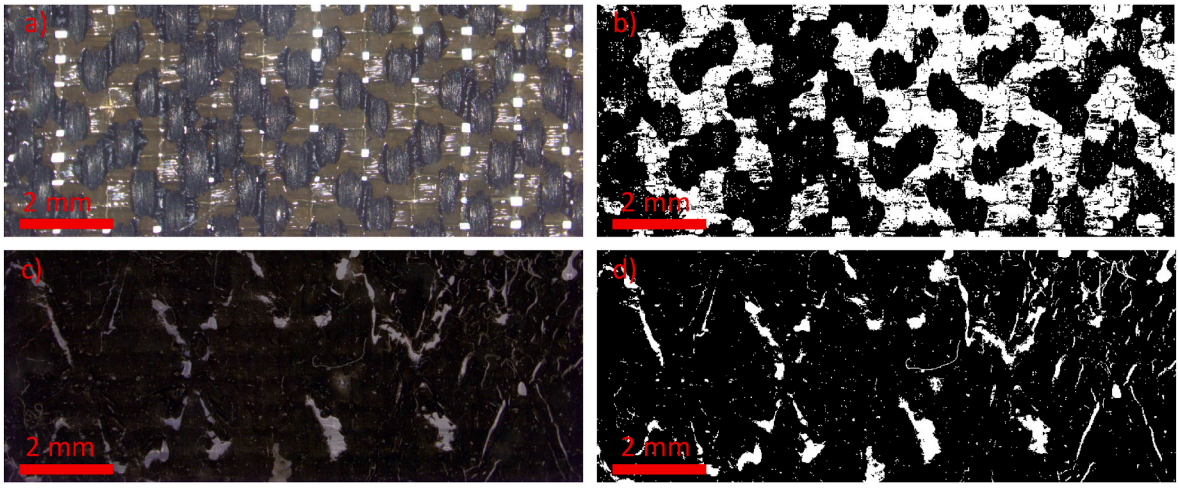

Fig. 4. Micrographs of prepreg surfaces after VACNT forest sample deposition and corresponding image analysis (White, non-deposited area. Black, CNT-deposited area.). a) 6376-prepreg, b) Image analysis 6376-prepreg, c) DeltaTech-prepreg, d) Image analysis DeltaTech-prepreg.

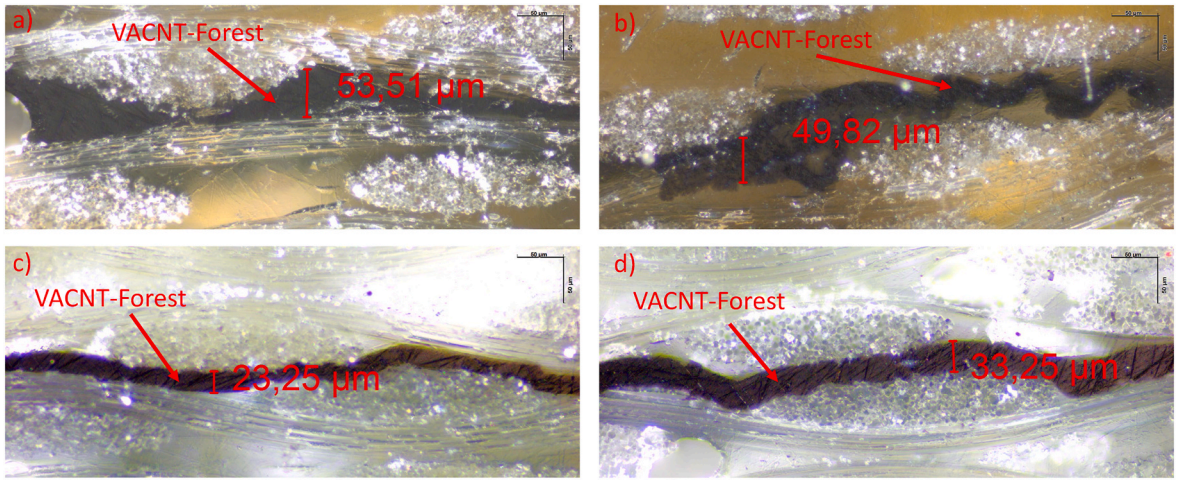

Fig. 5. Cross sections of samples, revealing the VACNT forest after curing. a) 6376-1 CNT, b) 6376-2 CNT, c) DeltaTech-1 CNT, d) DeltaTech-2 CNT.

alignment of the deposited forest. However, is should be noted that the deposited CNTs are cohesive and concentrated in a small region, not dispersing during the curing. Knowing the volume fraction of the VACNT forest, its deposition coverage, and now the thickness of the CNT-rich region, the volume fraction of CNTs in the epoxy of this region is calculated. In 6376-1 CNT, the volume fraction of CNTs is calculated to 0.17% (0.28 wt%) and in 6376–2 CNT 0.35% (0.60 wt%). The same procedure is performed on the DeltaTech samples, seen in Fig. 5c and d. However, here a continuous CNT-rich region with a continuous thickness is observed, containing only epoxy and CNTs. The average thickness is 19.68 µm (2.59 std) and 35.82 µm (3.42 std) in DeltaTech-1 CNT and DeltaTech-2 CNT, respectively. The volume fraction of CNTs in the CNT-rich region is calculated, to be 0.33% (0.61 wt%) and 0.36% (0.67 wt%) in DeltaTech-1 CNT and DeltaTech-2 CNT, respectively.

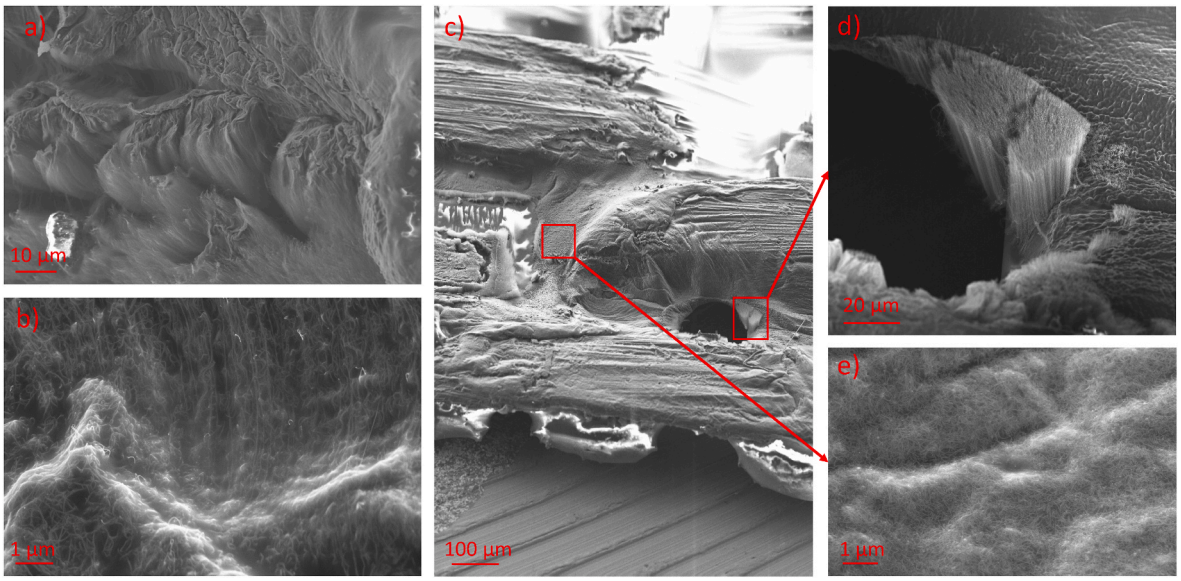

Fig. 6. SEM of prepreg surfaces after deposition of VACNT forest. a) fissure in DeltaTech-prepreg surface, b) magnification into fissure in DeltaTech surface. c) Surface of 6376-prepreg, d) and e) magnification of 6376-prepreg surface.

3.2. Morphology of VACNT forest after deposition

SEM micrographs of the prepreg surfaces after deposition of the VACNT forest is presented in Fig. 6. Viewing the surface of the DeltaTech-prepreg, no visible VACNT forests were seen at first, only revealing a uniform epoxy on top of the fibre bed. However, when finding fissures in the epoxy, the VACNT forest was visible, seen in Fig. 6a. A magnification into one of these fissures is presented in Fig. 6b. Here, individual CNTs are seen to have preserved their vertical alignment during after the deposition process. When viewing the 6376-prepreg surface, Fig. 6c, a more complex state of the deposition is observed. Epoxy from the top of the warp is seen to have been squeezed down from the top of the warp, to later accumulate below. A magnification of this epoxy is presented in Fig. 6e, revealing the CNTs in the epoxy to have lost their initial vertical alignment. Rather, the CNTs are now concentrated and entangled within a small volume of epoxy in the

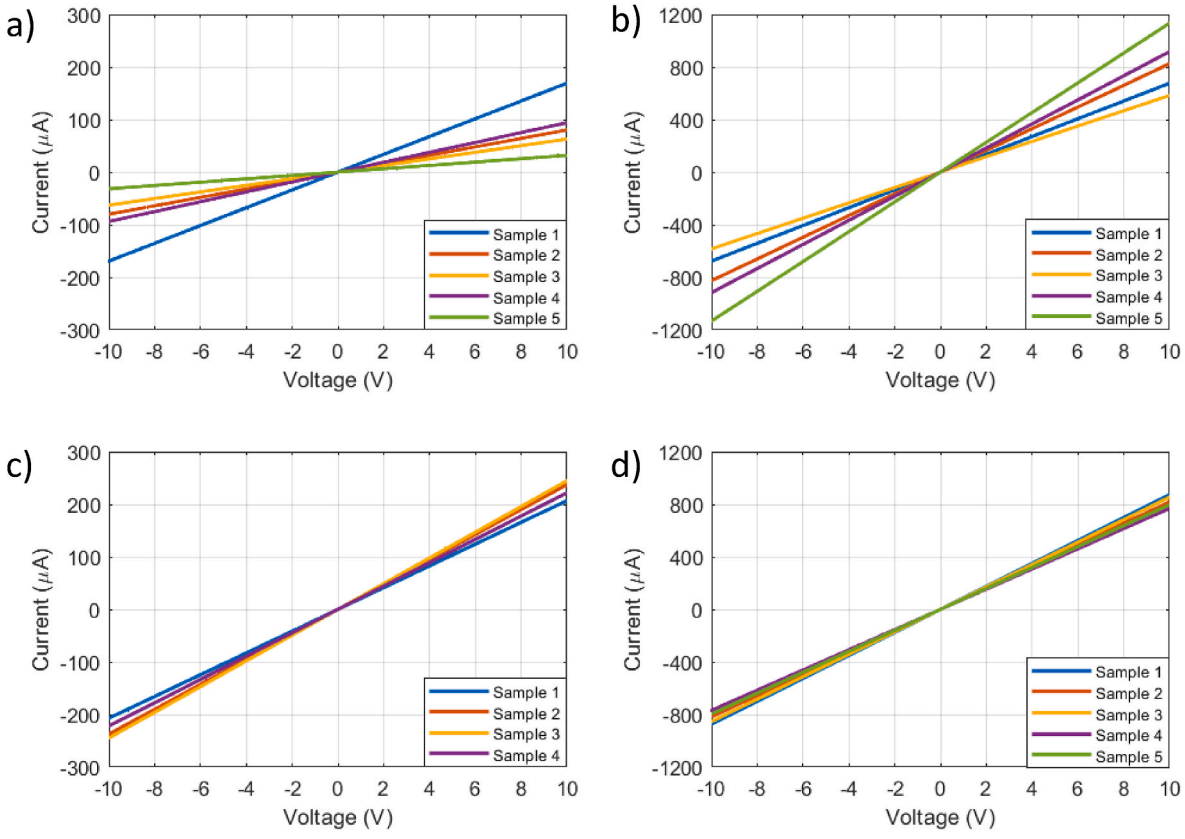

Fig. 7. Current-voltage sweeps of all samples. a) 6376-1 CNT, b) 6376-2 CNT, c) DeltaTech-1 CNT, d) DeltaTech-2 CNT.

depression of the prepreg. Instances of deposited VACNT forest which have preserved their original alignment were also found, seen in Fig. 6d. However, these locations are in the minority.

3.3. Electrical characterization

The current-voltage sweeps are presented in Fig. 7. All samples of the four sample types show a linear relation between the current and voltage, confirming their ohmic nature. The ohmic nature indicates a percolated network of CNTs, in which the current is conducted through metallic channels without semiconducting interconnects [45]. The calculated volume fractions of CNTs, section 3.1, in the CNT-rich regions are all above previously reported values of the percolation threshold of MWCNTs of similar aspect ratios (>1000) in epoxy, concluding the presence of a well percolated and conductive CNT network in all samples [46]. The resistance of each sample is calculated from the current-voltage sweeps. In Table 1 it is seen in that the samples of the 6376-sample type are more resistive and have a wider spread in measured resistance in comparison to their DeltaTech counterpart. As the resistance of the CNT-rich region is due to the percolated system of CNTs, the better deposition of the VACNT forest on the DeltaTech-prepreg provides more numerous conductive pathways which consequently lowers the resistance.

The stability of the samples' resistance is studied over 100 h at room temperature, presented in figure S2 in Supportive Information. No resistance drift was observed during this time, indicating no disruptions in the CNT network due to Joule heating [47].

3.4. Sensing evaluation

3.4.1. Temperature sensing

The thermoresistive behaviour of each sample type was studied, seen in Figs. 8 and 9. A negative resistance coefficient (NRC) behaviour is observed, the resistance decreasing with increased temperature. The previous results showing the ohmic nature of our samples, determining the presence of a thick percolated conductive network with metallic channels, justifies the thermoresistive response to be evaluated according to the fluctuation-assisted tunnelling (FAT) model [17]:

$$\frac{R}{R_0(T_0)} = \beta * \exp\left(\frac{T_b}{T_s + T}\right) \quad (1)$$

where R/R_0 is normalized resistance to a reference temperature, T_0. Thermal voltage fluctuations in the conductive network become large enough to affect the conductivity when energy of the electronic states reach the top of the barrier, $k_B T_B$. Thermal fluctuations commence to affect the conductivity of the system significantly from T_s and above. The ratio T_s/T_b indicates the remaining conductivity of the system towards absolute zero temperature. β is a prefactor [17,29,48]. The temperature-resistance data from a temperature cycle between −70 °C and 180 °C (200–450 K) is presented in Fig. 8 for the 6376–1 and −2 CNT samples, and in Fig. 9 the DeltaTech-1 and -2 CNT samples. Figs. 8 and 9 also include a curve according to the FAT-model, the fitting parameters presented in Table 2. The results indicate a great thermoresistive effect in the embedded VACNT forests. This could be exploited, by employing the embedded VACNT forests as temperature sensors. In the 6376 samples in Fig. 8, the exponential decay of resistance in response to increased temperature continues over the studied temperature range. However, in the DeltaTech samples, the resistance response changes at around 400 K (≈120 °C). This change is determined through differential scanning calorimetry (DSC) to correspond with the epoxy's glass transition temperature, T_g.

Table 1
Average resistance and standard deviation of each sample types.

	Average Resistance (kΩ)	Standard Deviation (kΩ)
6376-1 CNT	125.8	94.0
6376-2 CNT	12.7	3.3
DeltaTech-1 CNT	44.1	3.3
DeltaTech-2 CNT	12.2	0.6

3.4.2. Strain sensing

Tensile testing was performed to determine a) the sensitivity of the manufactured samples as strain gauges, and b) determine the range from which the VACNT forest could perform as a strain gauge. For the sensitivity, tensile testing by cycling twice between 0 and 10 kN was performed. To determine the measurement range, tensile testing of incremental steps of 100 N up to 1 kN was performed. The resistive responses of the four sample types when strained by 10 kN are presented in Fig. 10. It is seen that the embedded VACNT forest's piezoresistive response is linear and in phase to the measured strain of the sample. The signal remains stable under tension as 10 kN is held and no hysteresis of the signal is noted. Evaluating the sensitivity of resistive strain gauges, the gauge factor is used, given by:

$$GF = \frac{\Delta R/R_0}{\varepsilon} \quad (2)$$

where ΔR is the change in resistance over the strain range, R_0 the resistance of the unstrained sample and ε the measured strain. Calculating the gauge factor for each sample type, the 6376–1 and −2 CNT samples have gauge factors of 1.21 ± 0.01 and 1.19 ± 0.17, respectively. The DeltaTech-1 and -2 CNT samples have gauge factors of 1.22 ± 0.04 and 1.33 ± 0.04, respectively. All sample types have very similar gauge factors, the use of two VACNT forests instead of one not affecting the gauge factor significantly. In Fig. 11, the lower strain range limit of selected samples from the four sample types is presented. Increasing the load incrementally by 100 N each step, we observe in Figs. 11a and c the 6376–1 and DeltaTech-1 to have a piezoresistive response to strain as low as 9×10^{-3}% (100 N). However, this fine resolution to lower strains is not easily reproducible in all samples. Affected by noise in the measurements, a clear response to strain is not seen until 0.05% strain (500 N) in the majority of the samples. Further work refining the measurement method could perhaps alleviate this.

4. Discussion

The initial nanoscale studies of individual CNTs and the VACNT forest are essential. The outer diameter of individual CNTs being 8 ± 2 nm and the height of the forest being 20 μm determines the aspect ratio of individual CNTs to be 2000–3000. The aspect ratio of the used CNTs is of great significance to the percolated systems, requiring lower volume fractions to reach the percolation threshold. The calculated volume fractions of CNTs in the studied samples all surpass reported percolation thresholds using CNTs of similar aspect ratios (>1000) in epoxy [46]. The presence of a percolated system in the sample is evident by the clear ohmic behaviour of all samples seen during the current-voltage sweeps indicating a conductive network of metallic MWCNTs.

A characterization to evaluate the carbon fibre veil as contacting material has been performed, see figures S3 and S4 in Supportive Information. The characterization included current-voltage sweeps and strain measurements. The carbon fibre veil was determined to be ohmic in nature and poses low resistance, 27 Ω. This resistance is negligible to the resistance of the VACNT forest. In addition, the resistance shift is negligible when strained, 0.5 Ω. Therefore, it was concluded from this characterization that the carbon fibre veil was a suitable contacting material.

The preservation of the alignment of the VACNT forest after deposition has been seen in Fig. 6 to differ in the two used prepreg materials. As seen in fissures of the surface epoxy in the DeltaTech-prepreg, the alignment of the VACNT forest is preserved. As the VACNT forest is not visible elsewhere on the surface, it is concluded that the VACNT forest is

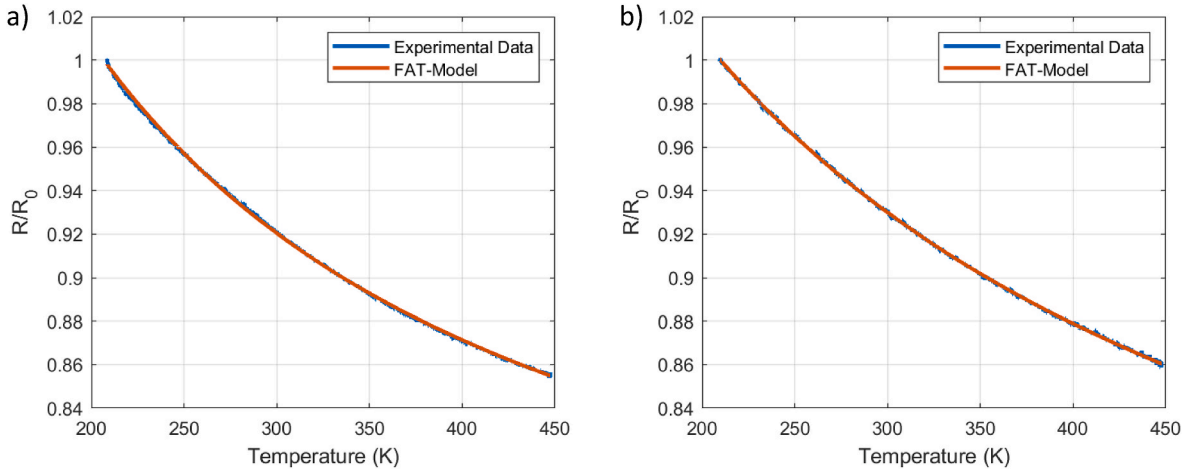

Fig. 8. Temperature sensing data and FAT-model curve fit for: a) 6376-1 CNT, b) 6376-2 CNT.

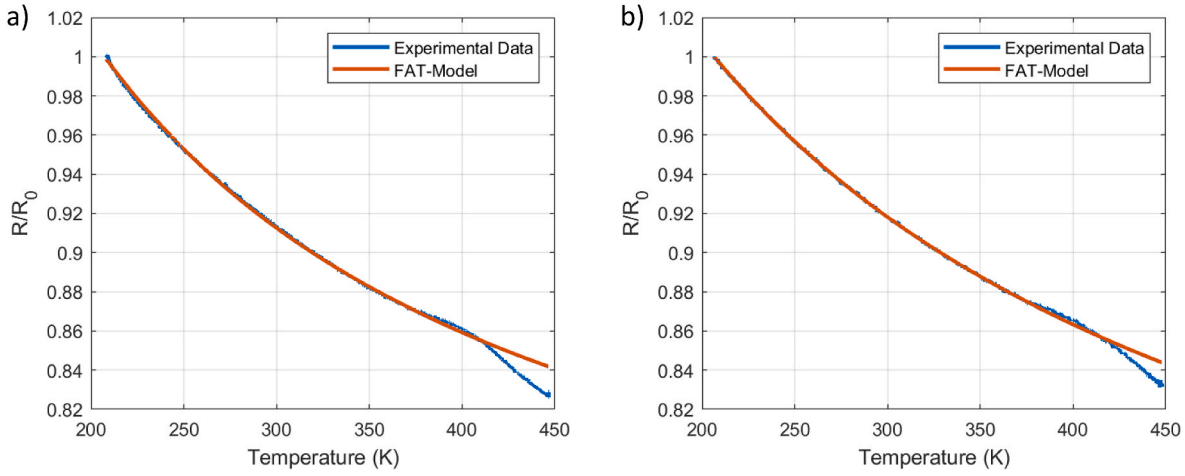

Fig. 9. Temperature sensing data and FAT-model curve fit for: a) DeltaTech-1 CNT, b) DeltaTech-2 CNT.

Table 2
Fitting parameters to the FAT-model, used in Figs. 8 and 9.

	T_b (K)	E_a (meV)	T_s (K)	T_s/T_b	β
6376-1 CNT	111.7	9.63	104.2	0.93	0.70
6376-2 CNT	194.6	16.77	238.9	1.23	0.65
DeltaTech-1 CNT	117.5	10.13	94.7	0.81	0.68
DeltaTech-2 CNT	181.5	15.64	195.2	1.08	0.64

fully infiltrated by epoxy in this material as we can optically verify, Fig. 4c, their presence. This finding, together with the determined thicknesses of the CNT-rich region in the cured state, Fig. 5c and d, implies a preservation of the alignment also in the cured state, as previously seen in work by Hallander et al. [49]. Seen in Fig. 6c and e, the alignment of the VACNT forest is seen to be disrupted to a large extent in the 6376-prepreg. As epoxy is squeezed down into the depressions of the 6376-prepreg, the CNTs are moved as well, resulting in an entangled architecture of CNTs seen in Fig. 6e. Although forests with preserved alignment are observed, Fig. 6d, these are in the minority. These findings explain well the irregular thickness and waviness of the CNT-rich region seen in the cross-sections of the cured samples seen in Fig. 5a and b. From these findings, the importance of the topology of the prepreg material to the quality of the deposition of the VACNT forest is revealed, favouring a flatter prepreg topology to preserve the alignment of the VACNT forest after deposition. Although the alignment may change during the deposition of VACNTs, the method assures a local enrichment of CNTs in the structure, not dispersing from its location of deposition. In addition, the method avoids the severe problems of CNT-agglomerations forming, which is a major concern when using CNTs of high aspect ratios in mixing operations to manufacture CNT-nanocomposites. Interestingly, the difference in alignment does not affect the sensitivity to strain in the different sample types, seen by the calculated gauge factors. In [23], their CNT-nanocomposites sensors manufactured by mixing epoxy and CNTs with 500–1500 in aspect ratio suffered severe agglomeration, forming large CNT aggregates. As a consequence, fewer conductive paths are formed across the sample, resulting in lower conductivity. Even our most resistive sample, having a 0.28 wt% of CNTs in the CNT-rich region has a higher conductivity, ≈0.6 S/m, than their most conductive sample, $4.5*10^{-2}$ S/m, having a CNT content of 15 wt%. This major difference in conductivity clarifies the advantage of using the VACNT forest architecture in comparison to the nanocomposite architecture.

The thermoresistive data showed a clear NRC behaviour. However, this is mostly seen in semiconducting materials. Typical metallic behaviour is characterized by increased resistance in response to increased temperature due to phonon-scattering events, which is seen in individual metallic SWCNTs [50] and thick SWCNT networks [45]. In the literature, the NRC behaviour of CNT-based temperature sensors is explained by variable-range hopping (VRH) or fluctuation-assisted tunnelling, previously abbreviated as FAT [17]. Often observed in

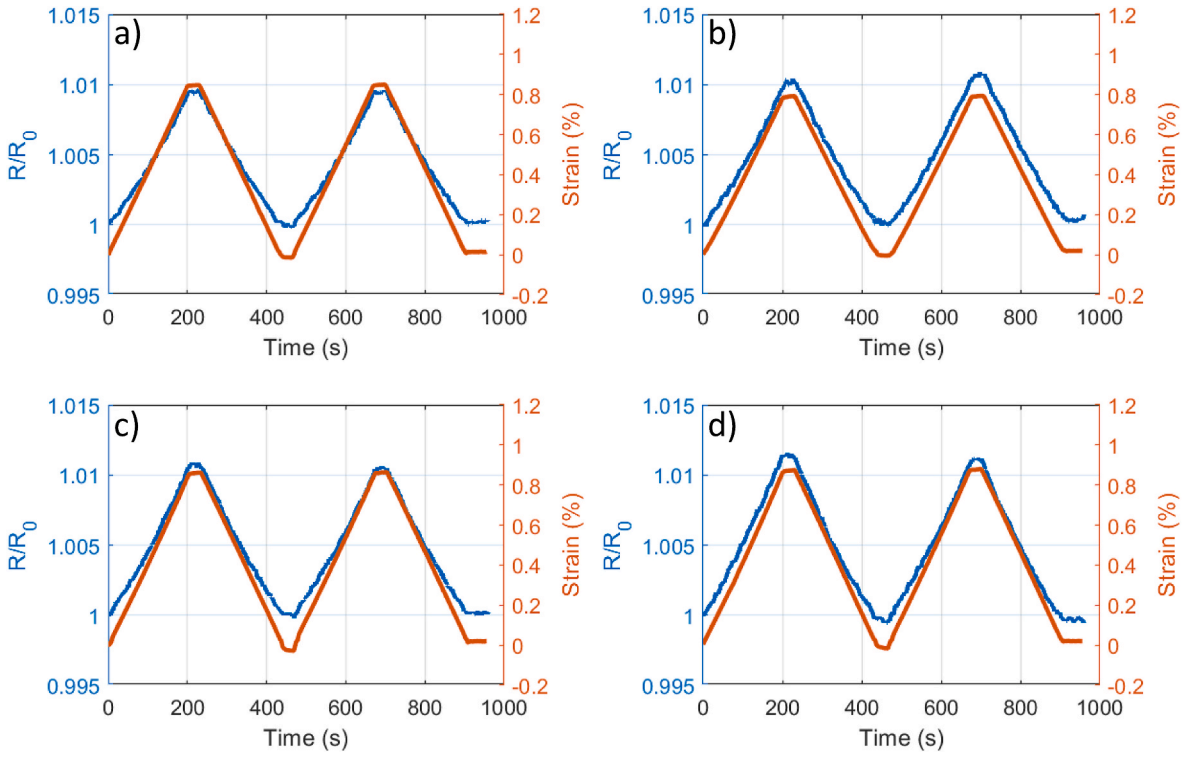

Fig. 10. Strain sensing of a) 6376-1 CNT, b) 6376-2 CNT, c) DeltaTech-1 CNT and d) DeltaTech-2 CNT, determining their gauge factor.

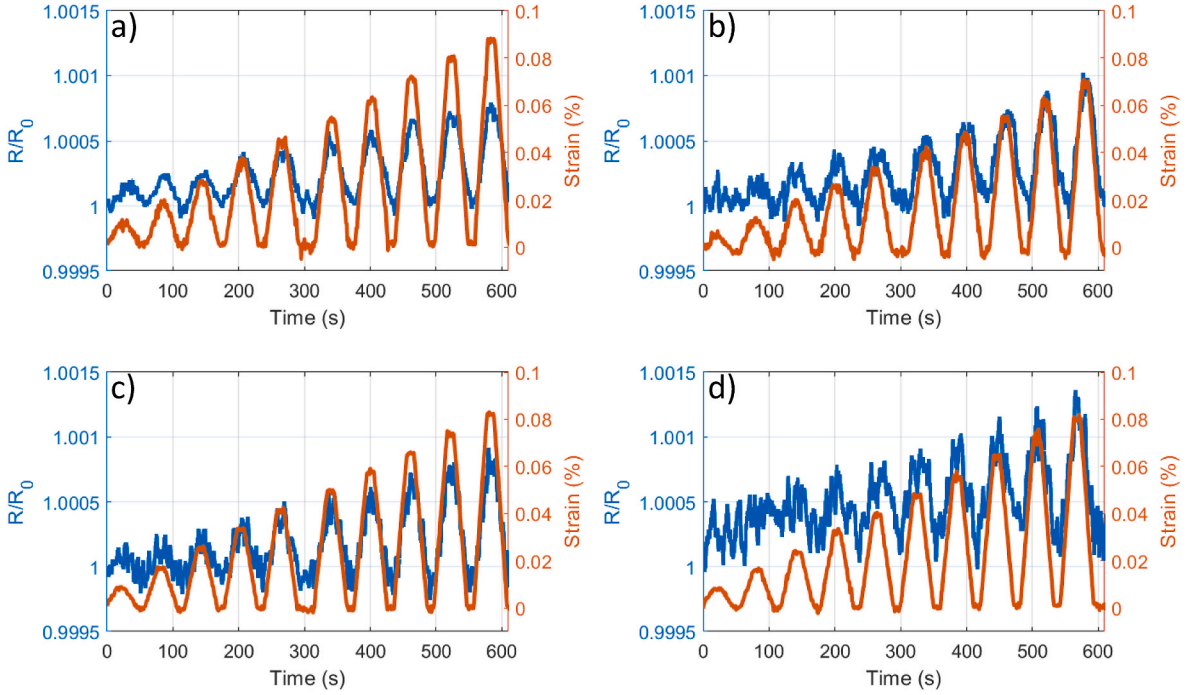

Fig. 11. Strain sensing of a) 6376-1 CNT, b) 6376-2 CNT, c) DeltaTech-1 CNT and d) DeltaTech-2 CNT, determining the sensing range.

semiconductors, VRH is characterized by hopping events between localized states for conduction. FAT is characterized by conduction through metallic channels, being surrounded by an insulating environment and tunnelling aided by thermal fluctuation between the metallic channels, hence why the conclusion FAT is the governing thermoresistive mechanism in our system. Which effect is prevalent in the CNT architecture depends on the volume fraction of CNTs in the percolated CNT network and whether SWCNTs or MWCNTs are used [18,45]. In this work, the tunnelling activation energies, E_a, correspond well to the work of Lee et al. [29] performing temperature measurements on vertically and horizontally aligned CNT forests. Through curve-fitting, they determined the activation energy of their forest to 14.2 meV, independent of the vertical or horizontal alignment. However, their value of T_s (6.1 K) is much smaller than ours, presented in Table 2. An

explanation for this has so far not been found. In [51], a high T_s/T_b ratio is stated to be present in more conductive systems of metallic character, whilst a low value is a sign of disordered semiconductors. Observing the curve-fit values in Table 2 and the average resistance in Table 1, this relation is only accurate when comparing the 6376-1 CNT versus −2 CNT and DeltaTech-1 CNT versus −2 CNT. The fact that this claim is not categorically applicable in embedded VACNT forests implies that other, yet unknown, effects affect the thermoresistive behaviour.

The origin of the piezoresistive effect in CNT/polymer-based sensors are i) change in tunnelling distance between CNTs [23,24,52], ii) the piezoresistive effect from individual CNTs [23,47] and/or iii) the break-up of conductive paths in the percolated system [53–55]. Which effect is dominant depends on the CNT-architecture, the aspect ratio of the CNTs, and the studied strain range. The majority of works studying the piezoresistive behaviour of CNT-nanocomposites attribute the sensing mechanism to the tunnelling mechanism between CNTs due to changes in distance between CNTs. However, the tunnelling equation expresses an exponential dependency of the resistance with regards to the distance change [56]. As the piezoresistive response is strictly linear in this work, the tunnelling-based sensing mechanism is discarded as the dominant sensing mechanism, even though tunnelling is present in the system due to the percolated network. Break-up of the percolated network is also unlikely as it is only attributed to higher strains, whereas in this work we are evaluating the linear-elastic region. Rather, the sensing mechanism of our sample is due to the piezoresistive effect present in individual CNTs [57] as they are deformed as the strain is applied to the sample. In their study, Yin et al. [23] reported the piezoresistive response of their nanocomposites using high aspect ratio CNTs to be due to the collective piezoresistive effect of individual CNTs. Yin et al. conclude in their study that the aspect ratio of their CNTs determines the piezoresistive mechanism of their nanocomposites, the low aspect ratio (>100) producing a tunnelling-dependent piezoresistivity, and the higher aspect ratio (500–1500) producing piezoresistivity due to inherent piezoresistivity of carbon nanotubes. This conclusion fits well to the used CNTs in our study, as the aspect ratio is ≈ 2000–3000. The aspect ratio of CNTs is important for stress transfer from the matrix to the CNTs, according to the shear-lag model [58], further improving the case of CNT piezoresistivity being accountable for the sample's piezoresistive response to strain. The piezoresistive effect of individual CNTs being the mechanism determining the piezoresistive response of the samples explains the similar gauge factors of all sample types. In contrast, the sensitivity of tunnelling-dependent strain gauges is heavily reliant on the volume fraction of CNTs, as sensitivity is the highest around the percolation threshold and less sensitive in the saturated region [24]. However, no such pattern is seen in this study. Similarly, the gauge factor of samples using high aspect ratio CNTs in [23] doesn't follow a trend with sensitivity being dependent on the weight fraction of CNTs in the nanocomposite. However, the calculated gauge factors of the studied samples in this study (1.19–1.33) are lower than those of Yin et al. (3.8–4.3). Although the studied VACNT forest architecture has a low gauge factor, comparable to resistive foils, gauge factor≈2, the studied VACNT forest architecture as a strain gauge has many advantages over other CNT architectures. The VACNT forest offers the possibility to deposit CNTs of high aspect ratio locally, avoiding issues with severe agglomeration, ensuring good conductivity with low CNT-loading. The VACNT forest architecture and deposition method ensures consistency of conductivity and gauge factor in manufactured samples. The collective piezoresistive response from individual high aspect ratio CNTs causes the piezoresistivity of the samples on the mesoscale. Finally, the embedded VACNT forest architecture gives rise to a linear, non-changing, piezoresistivity not seen in other works of CNT architectures embedded into structural composites.

5. Conclusion

Embedded VACNT forests into glass fibre/epoxy structural composite are shown to possess excellent sensing abilities to temperature and strain. The observed linear piezoresistivity of all samples is insensitive to the different prepreg-materials used, the volume fraction of CNTs and the resistivity of the system. Through the multiscale approach, studying the VACNT forest and its constituent tubes on the nanoscale, up to the sensing abilities of the manufactured sample on the mesoscale, it is concluded that these piezoresistive properties are due to the intrinsic piezoresistivity of the individual tubes. This characteristic of the VACNT forest offers the possibility to manufacture embedded strain sensors with a predictable sensitivity to strain. The observed thermoresistive behaviour of the embedded VACNT forest is determined to be due to fluctuation-assisted tunnelling, making it a suitable temperature sensor at temperatures lower than the T_g of the host matrix. To explain the sensing behaviour in response to both strain and temperature, the multiscale approach has proven to be essential. When designing CNT-based sensors, knowledge of individual CNTs, CNT-network architecture and manufacturing methods is essential to bridge the gap between nanoscale properties and mesoscale functionalities.

CRediT statements

Tobias Karlsson: Writing – Original Draft, Writing – Review & Editing, Investigation, Methodology, Conceptualization, Validation, Visualization, Resources, Per Hallander: Writing – Original Draft, Writing – Review & Editing, Investigation, Methodology, Conceptualization, Resources, Supervision, Project administration, Funding acquisition, Fang Liu: Investigation, Methodology, Resources Thirza Poot: Investigation, Methodology, Resources, Malin Åkermo: Writing – Original Draft, Writing – Review & Editing, Methodology, Conceptualization, Resources, Supervision, Project administration, Funding acquisition.

Declaration of competing interest

The authors declare that they have no known competing financial interests or personal relationships that could have appeared to influence the work reported in this paper.

Data availability

Data will be made available on request.

Acknowledgements

The authors would like to thank the Swedish Governmental Agency for Innovation Systems, Vinnova, through the IntDemo program, Strategic Innovation Program LIGHTer and LIGHTer Academy, and SAAB AB for supporting this research. This research was partially sponsored by XPRES (Centre of Excellence in Production Research – a strategic research area in Sweden. Special thanks to Tijana Todorovic at KTH, for her assistance in performing TGA and DSC measurements.

Appendix A. Supplementary data

Supplementary data to this article can be found online at https://doi.org/10.1016/j.compositesb.2023.110587.

References

[1] Iijima S. Helical microtubules of graphitic carbon. Nature 1991;354:56–8.
[2] Saito R, Fujita M, Dresselhaus G, Dresselhaus MS. Electronic structure of chiral graphene tubules. Appl Phys Lett 1992;60(18):2204–6.
[3] Hamada N, Sawada S, Oshiyama A. New one-dimensional conductors: graphitic mictrotubules. Phys Rev Lett 1992;68(10):1579–81.
[4] Wei BQ, Vajtai R, Ajayan PM. Reliability and current carrying capacity of carbon nanotubes. Appl Phys Lett 2001;79(8):1172–4.
[5] Bachtold A, Fuhrer MS, Plyasunov S, Forero M, Anderson EH, Zettl A, et al. Scanned probe microscopy of electronic transport in carbon nanotubes. Phys Rev Lett 2000;84(26):6082–5.

[6] Tans SJ, Devoret MH, Dai H, Thess A, Smalley RE, Geerligs L, et al. Individual single-wall carbon nanotubes as quantum wires. Nature 1997;386:474–7.
[7] White C, Todorov TN. Carbon nanotubes as long ballistic conductors. Nature 1998; 393:240–2.
[8] Javey A, Guo J, Wang Q, Lundstrom M, Dai H. Ballistic carbon nanotube field-effect transistors. Nature 2003;424:654–7.
[9] Zhang Z, Liang X, Wang S, Yao K, Hu Y, Zhu Y, et al. Doping-free fabrication of carbon nanotube based ballistic CMOS devices and circuits. Nano Lett 2007;7(12): 3603–7.
[10] Frank S, Poncharal P, Wang ZL, Heer WA De. Carbon nanotube quantum resistors. Science 1998;280(5370):1744–6.
[11] Berger C, Yi Y, Wang ZL, De Heer WA. Multiwalled carbon nanotubes are ballistic conductors at room temperature. Appl Phys A 2002;74(3):363–5.
[12] Li HJ, Lu WG, Li JJ, Bai XD, Gu CZ. Multichannel ballistic transport in multiwall carbon nanotubes. Phys Rev Lett 2005;95(8):086601.
[13] Poncharal P, Berger C, Yi Y, Wang ZL, De Heer WA. Room temperature ballistic conduction in carbon nanotubes. J Phys Chem B 2002;106(47):12104–18.
[14] Langer L, Bayot V, Grivei E, Issi JP, Heremans JP, Olk CH, et al. Quantum transport in a multiwalled carbon nanotube. Phys Rev Lett 1996;76(3):479–82.
[15] Avouris P, Chen Z, Perebeinos V. Carbon-based electronics. Nat Nanotechnol 2007; 2:605–15.
[16] Bourlon B, Miko C, Forró L, Glattli DC, Bachtold A. Determination of the intershell conductance in multiwalled carbon nanotubes. Phys Rev Lett 2004;93(17):176806.
[17] Kaiser AB. Electronic transport properties of conducting polymers and carbon nanotubes. Rep Prog Phys 2001;64(1):1–49.
[18] Kaiser AB, Skákalová V. Electronic conduction in polymers, carbon nanotubes and graphene. Chem Soc Rev 2011;40(7):3786–801.
[19] Kim SY, Jee E, Kim JS, Kim DH. Conformable and ionic textiles using sheath-core carbon nanotube microyarns for highly sensitive and reliable pressure sensors. RSC Adv 2017;7(38):23820–6.
[20] Lu S, Chen D, Wang X, Xiong X, Ma K, Zhang L, et al. Monitoring the glass transition temperature of polymeric composites with carbon nanotube buckypaper sensor. Polym Test 2017;57:12–6.
[21] Lu S, Zhao C, Zhang L, Chen D, Chen D, Wang X, et al. Real time monitoring of the curing degree and the manufacturing process of fiber reinforced composites with a carbon nanotube buckypaper sensor. RSC Adv 2018;8(39):22078–85.
[22] Lasater KL, Thostenson ET. In situ thermoresistive characterization of multifunctional composites of carbon nanotubes. Polymer 2012;53(23):5367–74.
[23] Yin G, Hu N, Karube Y, Liu Y, Li Y. A carbon nanotube/polymer strain sensor with linear and anti-symmetric piezoresistivity. J Compos Mater 2011;45(12):1315–23.
[24] Hu N, Karube Y, Arai M, Watanabe T, Yan C, Li Y, et al. Investigation on sensitivity of a polymer/carbon nanotube composite strain sensor. Carbon 2010;48(3):680–7.
[25] Oliva-Avilés A, Avilés F, Sosa V. Electrical and piezoresistive properties of multi-walled carbon nanotube/polymer composite films aligned by an electric field. Carbon 2011;49(9):2989–97.
[26] Avilés F, May-Pat A, Canché-Escamilla G, Rodríguez-Uicab O, Ku-Herrera JJ, Duarte-Aranda S, et al. Influence of carbon nanotube on the piezoresistive behavior of multiwall carbon nanotube/polymer composites. J Intell Mater Syst Struct 2016; 27(1):92–103.
[27] Shin UH, Jeong DW, Park SM, Kim SH, Lee HW, Kim JM. Highly stretchable conductors and piezocapacitive strain gauges based on simple contact-transfer patterning of carbon nanotube forests. Carbon 2014;80:396–404.
[28] Koratkar N, Modi A, Lass E, Ajayan P. Temperature effects on resistance of aligned multiwalled carbon nanotube films. J Nanosci Nanotechnol 2004;4(7):744–8.
[29] Lee J, Stein IY, Devoe ME, Lewis DJ, Lachman N, Kessler SS, et al. Impact of carbon nanotube length on electron transport in aligned carbon nanotube networks. Appl Phys Lett 2015;106(5):053110.
[30] Doshi SM, Thostenson ET. Thin and flexible carbon nanotube-based pressure sensors with ultrawide sensing range. ACS Sens 2018 Jul 27;3(7):1276–82.
[31] Luo S, Obitayo W, Liu T. SWCNT-thin-film-enabled fiber sensors for lifelong structural health monitoring of polymeric composites - from manufacturing to utilization to failure. Carbon 2014;76:321–9.
[32] Luo S, Wang Y, Wang G, Wang K, Wang Z, Zhang C, et al. CNT enabled Co-braided smart fabrics: a new route for non-invasive, highly sensitive &large-area monitoring of composites. Sci Rep 2017;7:44056.
[33] Dai H, Thostenson ET, Schumacher T. Comparative study of the thermoresistive behavior of carbon nanotube-based nanocomposites and multiscale hybrid composites. Compos B Eng 2021;222:109068.
[34] Yoo KP, Lim LT, Min NK, Lee MJ, Lee CJ, Park CW. Novel resistive-type humidity sensor based on multiwall carbon nanotube/polyimide composite films. Sensors Actuators, B Chem. 2010;145(1):120–5.
[35] Boztepe S, Liu H, Heider D, Thostenson ET. Novel carbon nanotube interlaminar film sensors for carbon fiber composites under uniaxial fatigue loading. Compos Struct 2018;189:340–8.
[36] Aly K, Li A, Bradford PD. Strain sensing in composites using aligned carbon nanotube sheets embedded in the interlaminar region. Composer Part A Appl Sci Manuf 2016;90:536–48.
[37] Garcia EJ, Wardle BL, John Hart A. Joining prepreg composite interfaces with aligned carbon nanotubes. Composer Part A Appl Sci Manuf 2008;39(6):1065–70.
[38] Conway H, Gouldstone C. Vertically aligned carbon nanotubes as interlaminar reinforcement in carbon fiber composite laminates. In: Proceedings of AIAA Scitech 2019 Forum. San Diego; January, 2019. p. 1–6.
[39] Hart AJ, Slocum AH. Force output, control of film structure, and microscale shape transfer by carbon nanotube growth under mechanical pressure. Nano Lett 2006;6 (6):1254–60.
[40] Egerton RF, Li P, Malac M. Radiation damage in the TEM and SEM. Micron 2004;35 (6):399–409.
[41] Mansfield E, Kar A, Hooker SA. Applications of TGA in quality control of SWCNTs. Anal Bioanal Chem 2010;396:1071–7.
[42] Bom D, Andrews R, Jacques D, Anthony J, Chen B, Meier MS, et al. Thermogravimetric analysis of the oxidation of multiwalled carbon nanotubes: evidence for the role of defect sites in carbon nanotube chemistry. Nano Lett 2002; 2(6):615–9.
[43] Mahajan A, Kingon A, Kukovecz Á, Konya Z, Vilarinho PM. Studies on the thermal decomposition of multiwall carbon nanotubes under different atmospheres. Mater Lett 2013;90:165–8.
[44] Liu Y, Ba H, Nguyen DL, Ersen O, Romero T, Zafeiratos S, et al. Synthesis of porous carbon nanotubes foam composites with a high accessible surface area and tunable porosity. J Mater Chem A 2013;1:9508–16.
[45] Skákalová V, Kaiser AB, Woo YS, Roth S. Electronic transport in carbon nanotubes: from individual nanotubes to thin and thick networks. Phys Rev B 2006;74(8): 085403.
[46] Bauhofer W, Kovacs JZ. A review and analysis of electrical percolation in carbon nanotube polymer composites. Compos Sci Technol 2009;69(10):1486–98.
[47] Li A, Bogdanovich AE, Bradford PD. Aligned carbon nanotube sheet piezoresistive strain sensors. Smart Mater Struct 2015;24(9):095004.
[48] Sheng P. Fluctuation-induced tunneling conduction in disordered materials. Phys Rev B 1980;21(6):2180–95.
[49] Hallander P, Sjölander J, Åkermo M. Forming of composite spars including interlayers of aligned , multiwall , carbon nanotubes : an experimental study. Polym Compos 2018;39(1):181–91.
[50] Kane CL, Mele EJ, Lee RS, Fischer JE, Petit P, Dai H. Temperature-dependent resistivity of single-wall carbon nanotubes. Europhys Lett 1998;41(6):683–8.
[51] Skákalová V, Kaiser AB, Hrnc K, Roth S. Effect of chemical treatment on electrical conductivity , infrared absorption , and Raman spectra of single-walled carbon nanotubes. J Phys Chem B 2005;109(15):7174–81.
[52] Hu N, Karube Y, Yan C, Masuda Z, Fukunaga H. Tunneling effect in a polymer/carbon nanotube nanocomposite strain sensor. Acta Mater 2008;56(13):2929–36.
[53] Gallo GJ, Thostenson ET. Electrical characterization and modeling of carbon nanotube and carbon fiber self-sensing composites for enhanced sensing of microcracks. Mater Today Commun 2015;3:17–26.
[54] Gao L, Chou TW, Thostenson ET, Zhang Z. A comparative study of damage sensing in fiber composites using uniformly and non-uniformly dispersed carbon nanotubes. Carbon 2010;48(13):3788–94.
[55] Gao L, Chou TW, Thostenson ET, Zhang Z, Coulaud M. In situ sensing of impact damage in epoxy/glass fiber composites using percolating carbon nanotube networks. Carbon 2011;49(10):3382–5.
[56] Li C, Thostenson ET, wei Chou T. Dominant role of tunneling resistance in the electrical conductivity of carbon nanotube – based composites. Appl Phys Lett 2007;91:223114.
[57] Tombler TW, Zhou C, Alexseyev L, Kong J, Dai H. Reversible electromechanical characteristics of carbon nanotubes under local-probe manipulation. Nature 2000; 405:769–72.
[58] Theodosiou TC, Saravanos DA. Numerical investigation of mechanisms affecting the piezoresistive properties of CNT-doped polymers using multi-scale models. Compos Sci Technol 2010;70(9):1312–20.